Radiometric Enhancement of Landsat 8 OLI Imagery Using Coastal/Aerosol Band

by Syam'ani Syam'ani

Radiometric Enhancement of Landsat 8 OLI Imagery Using Coastal/Aerosol Band

Syam'ani
Faculty of Forestry
University of Lambung Mangkurat
Banjarbaru, Indonesia
syamani.fhut@ulm.ac.id

Abstract— The presence of atmospheric particles in multispectral imageries such as Landsat 8 OLI can reduce the visual acuity of the imageries. The most ideal method to reduce the existence of atmospheric particles in the imagery, as well as to enhance the visual appearance of the imagery, is to employ atmospheric corrections. However, atmospheric corrections are a very complex process. Besides, sometimes the results don't really have an impact visually. There are many other methods to enhance an imagery radiometrically, either by stretching the pixel value, shifting the histogram, or reducing the presence of clouds. This research aims to develop practical formulations to enhance the spectral value of the Landsat 8 OLI imagery bands, by reducing the presence of aerosol particles using the C/A band. Several regression models were involved in the construction process of these formulations. The accuracy assessment was performed using the Pearson correlation coefficient and RMSE, using the USGS Landsat 8 OLI TOC imagery as a comparison. The results showed that the radiometric imagery enhancement using the C/A band gave satisfactory results. Apart from providing a significant visual sharpness increase, for the exponential model with parameters, the average Pearson correlation coefficient is 0.96, with an RMSE value of 0.04, relative to the USGS Landsat 8 OLI TOC product. For a more practical model, we can omit the parameters in the exponential model. The results that will be obtained are still quite accurate. Furthermore, we can implement this enhancement model directly on digital numbers.

Keywords: radiometric enhancement, atmospheric correction, Landsat 8 OLI, coastal aerosol, spectral indices

I. INTRODUCTION

The visible bands on multispectral imageries such as the Landsat 8 Operational Land Imager (OLI), are visually the bands most problematic with radiometric acuity. This is because the visible bands have short wavelengths, making them most vulnerable to atmospheric disturbances, such as dust, haze, and clouds. So that in general, the appearance of the features in the composite imagery of the visible bands will appear darker.

A practical solution for visual feature identification, perhaps, is to create a composite imagery using bands that have a longer wavelength. Such as Near Infrared (NIR) or Short Wave Infrared (SWIR) bands. Because NIR and SWIR have longer wavelengths, so that atmospheric disturbances are minimized. As a result, the feature appearance on NIR and SWIR tends to be sharper than the visible band.

However, sometimes certain features are easier to identify visually in visible bands. For example, to distinguish between buildings and bare lands, it will be easier to see in Landsat 8 composite 4,3,2, than in Landsat 8 composite 6,5,4 for example. Because in composite 4,3,2 (true color composite), the roof of the building will show the original color as the color of the object that we see directly in the field. Meanwhile, the Landsat 8 composite of 6,5,4 (false color composite), the color of the roof of the building and the color of the bare lands tend to be the same. Despite the fact, the features of the composite 6,5,4 are much clearer when compared to composite 4,3,2.

One of the reasons why the appearance of the features in the imagery looks darker, especially in the visible bands, is due to atmospheric interference. Therefore, one technique to enhance visible bands or other bands is to reduce or eliminate atmospheric disturbances from the imagery. The most ideal method for reducing atmospheric disturbances is by employing atmospheric correction.

Various methods of atmospheric correction have been developed. Starting from methods with image based approach, such as Dark Objects Subtraction (DOS) [31][32][48], Empirical Line Method (ELM) [16], and histogram matching [35]. Up to complex methods based on physical models, such as 6S [13], 6SV [13][36] [41], Atmospheric Correction (ATCOR) [35], Landsat Ecosystem Disturbance Adaptive Processing System (LEDAPS) [22], Land Surface Reflectance Code (LaSRC) [15], MODTRAN4 [2], Fast Line-of-sight Atmospheric Analysis of Spectral Hypercubes (FLAASH) [27], Framework for Operational Radiometric Correction for Environmental monitoring (FORCE) [12], and Image Correction (iCOR) or OPERA [39]. Although very ideal, atmospheric corrections are very complex processes. Besides, sometimes the results don't really have an impact visually.

Another technique for increasing the radiometric sharpness of the visible bands is by stretching the imagery pixel values. Either linear stretching, non-linear stretching, or histogram modification [20][30][44]. This method is quite practical, but has risks. Especially if the atmospheric disturbance is severe. For example, the presence of a large enough cloud. In case of the presence of a large number of clouds or brightly colored objects, the pixel value stretching method often fails. Because the cloud itself or other bright objects will get sharper and seem to get bigger. This is because when we stretch the pixel value of the

imagery, the pixel value of the aerosol particles is also stretched.

Another potential method to increase the radiometric sharpness is to remove cirrus clouds from the imagery. Cirrus clouds form primarily in the upper troposphere, above about 8 km, where temperatures are generally below -30° C [3]. In a multispectral imagery like Landsat 8, this cloud type generally looks like a white mist with a smooth texture. The presence of cirrus clouds can sometimes darken the appearance of the features on the multispectral imageries. Reference [28] developed a method for removing cirrus clouds in Landsat 8 imagery, using the Cirrus bands available in Landsat 8. Unfortunately, this method is only effective for cirrus clouds. As for other types of clouds, or other atmospheric disturbances, this method does not have any effect.

As the last generation of the Landsat series. The Landsat 8 OLI has a number of new technological features. Among them is the existence of the Coastal/Aerosol (C/A) band [10][23]. The C/A band on Landsat 8 OLI is a band that has a spectrum range of 0.433 - 0.453 μm [10][23]. Meanwhile the Landsat 8 OLI blue band has a spectrum range of 0.450 - 515 μm [10][23]. Therefore, the C/A band has a shorter wavelength than the blue band. So that the C/A band is also called the ultra blue band [38]. Because it has the shortest wavelength of all OLI bands, C/A is the band most susceptible to aerosol particle interference. In other words, the C/A band stores the spectral value of aerosol particles in the greatest quantity among all OLI bands. The concentration of the spectral value of the aerosol particles which is quite dense in the C/A band has the potential to be used to reduce the presence of aerosol particles in other bands in the Landsat 8 OLI imagery.

The C/A band can be used for the characterization of aerosol optical properties when removing atmospheric effects over land targets [29]. Reference [15] use the C/A band for atmospheric correction. Because C/A is particularly helpful for retrieving aerosol properties, as it covers shorter wavelengths than the conventional Landsat, TM and ETM+ blue bands [15].

This research aims to develop some practical formulations to enhance the spectral value of the Landsat 8 OLI imagery bands, by reducing the presence of aerosol particles using the Coastal/Aerosol (C/A) band.

II. METHOD DEVELOPMENT

The basic concept of the method developed in this research is that the spectral value of aerosol particles in each band other than C/A is reduced by the spectral value of the aerosol particles in the C/A band. So that the presence of the spectral value of aerosol particles in other bands in the Landsat 8 imagery can be reduced. This method is actually inspired by the Normalized Difference Spectral Index (NDSI), such as the Normalized Difference Vegetation Index (NDVI) [24] or the Normalized Difference Water Index (NDWI) [6][19][37].

NDVI enhances vegetation features by reducing the spectral value of non-vegetation features by using a band that is sensitive to water and soil features (red band) as a sub-factor. Meanwhile, NDWI enhances water features by reducing the spectral value of non-water objects by using

bands that are sensitive to vegetation and soil features (NIR or SWIR bands) as sub-factors. By compiling an NDSI formula that is similar to NDVI and NDWI, where the C/A band is used as a subtractor, it is hoped that it will reduce the presence of atmospheric particle spectral values and enhance the spectral values of other bands on Landsat 8 OLI.

Therefore, the basic formula developed in this research is as follows:

$$\rho_i' = \frac{\rho_i - \rho_{ca}}{\rho_i + \rho_{ca}} \qquad (1)$$

Where:

ρ_i': the spectral value of band i enhanced

ρ_i: the spectral value of band i (band other than C/A)

ρ_{ca}: the spectral value of the C/A band

Visually, the transformation result from (1) is effective for reducing the aerosol particles in any of the other OLI bands. There is one problem, because an NDSI transformation will generally produce a spectral value in the range of -1 to 1. This is not a typical spectral (reflectance) value. Moreover, negative values have the potential to complicate some further analysis, such as square root operations. So that the transformed value can be stretched, for example to be 0 to 1. By using the following formula:

$$\rho_i' = \frac{\frac{\rho_i - \rho_{ca}}{\rho_i + \rho_{ca}} - (-1)}{1 - (-1)} \qquad (2)$$

$$\rho_i' = \frac{\frac{\rho_i - \rho_{ca}}{\rho_i + \rho_{ca}} + \frac{\rho_i + \rho_{ca}}{\rho_i + \rho_{ca}}}{2} \qquad (3)$$

$$\rho_i' = \frac{2\rho_i}{2(\rho_i + \rho_{ca})} \qquad (4)$$

$$\rho_i' = \frac{\rho_i}{\rho_i + \rho_{ca}} \qquad (5)$$

Equation (5) will give a typical spectral value for reflectance, which is from 0 to 1. However, another new problem arises here. Considering that (5) is a non-linear transformation, the spectral value of the transformed imagery has the potential to lose integrity. To solve this problem, the output of (5) must be transformed back to be linear the original TOA value. Linear is meant here is linear in terms of the spectral value of the surface features

In order to convert the transformed imagery's spectral value to linear to the original spectral value, we must first investigate the correlation between the transformed imagery of (5) and the Top of Atmosphere (TOA) reflectance value. For this purpose, a number of regression models can be used. Such as linear, exponential, logarithmic, polynomial, and power.

In the process of this investigation, a number of samples (region of interest) are required, to build a correlation model between the original TOA reflectance spectral value and the TOA reflectance spectral value resulting from the transformation of (5). Of course, the sample in the imagery must be selected for any spectral classes in clear regions from atmospheric disturbances. These spectral classes represent the basic objects in the multispectral imagery,

namely vegetation features, urban and bare land features, and water features.

III. IMPLEMENTATION AND RESULTS

The imagery used in this research is the Landsat 8 OLI imagery level-1, path/row 117/062, acquired on April 22, 2015. The accuracy assessment for the method developed in this research was carried out by comparing the spectral value of the transformed results, with Top of Canopy (TOC) reflectance. In this case, TOC is considered as ground truth reflectance. The comparison method used is Pearson correlation coefficient (r) [25] and Root Mean Square Error (RMSE) [1][21]. Which are formulated as follows:

$$r = \frac{\sum_{i=1}^{n}(x_i - \bar{x})(y_i - \bar{y})}{\sqrt{\sum_{i=1}^{n}(x_i - \bar{x})^2}\sqrt{\sum_{i=1}^{n}(y_i - \bar{y})^2}} \quad (6)$$

$$RMSE = \sqrt{\sum_{i=1}^{n}\frac{(x_i - y_i)^2}{n}} \quad (7)$$

Where:

x_i: the ith enhanced Landsat 8 band
y_i: the ith USGS Landsat 8 TOC band
n: number of sample pixels

Landsat 8 OLI level-2 imageries in TOC had been provided by USGS and can be downloaded for free from the website https://earthexplorer.usgs.gov. This Landsat 8 OLI imagery is atmospheric corrected using the LaSRC [11][15] method. Of course, in the process of accuracy assessment, the Landsat 8 OLI level-2 (surface reflectance) imagery selected is the same acquisition imagery as the Landsat 8 OLI level-1 imagery used to build the model. Namely path/row 117/062 acquired on April 22, 2015.

In this research, the enhancement process was carried out on the TOA reflectance. So that the Landsat 8 OLI imagery is first calibrated into TOA reflectance. Based on the results of the correlation investigation between the bands transformed by (5) with the TOA reflectance bands, it turns out that the correlation between the transformed spectral value of (5) and the original TOA reflectance value on the bands appears to be power. The details can be seen in Table I. The actual high correlation varies between exponential, polynomial, and power. However, for convenience, we generalize to exponential and power. Because the exponential and power correlation look strong for all OLI bands. The polynomial generally has a high correlation coefficient, but the value drop on the SWIR 1 band. Furthermore, we do not recommend the polynomial model due to the complexity of the equation.

Therefore, to convert the spectral value transformed by (5) to be linear to the original TOA reflectance value, the general formulas are as follows:

$$\rho_i' = \alpha_i e^{\beta_i\left(\frac{\rho_i}{(\rho_i + \rho_{ca})}\right)} \quad (8)$$

Or

$$\rho_i' = \alpha_i\left(\frac{\rho_i}{(\rho_i + \rho_{ca})}\right)^{\beta_i} \quad (9)$$

Where:

ρ_i': the spectral value of band i enhanced
ρ_i: the spectral value of band i (band other than C/A)
ρ_{ca}: the spectral value of the C/A band
α_i and β_i: parameters for band i (band other than C/A)
e: the natural logarithm number 2.71828182845905

Here the parameters α_i and β_i in (8) and (9) are determined using a number of regions of interest (ROI), in the area that is clearest from atmospheric disturbances in the imagery. ROIs were selected stratifiedly in several spectral classes, namely Dense Vegetation, Medium Vegetation, Sparse Vegetation, Urban and Bare lands, and Water Bodies. Dense Vegetation includes Dense Dryland Forest, Dense Swamp Forest, and Peatland Forest. Medium Vegetation includes Mixed Garden, Palm Oil Plantations, Peatland Shrub and Bushes, Rubber Plantations, Sparse Dryland Forest, and Sparse Swamp Forest. Sparse Vegetation includes Grass, Shrub and Bushes, Swamp Grass, and Swamp Shrub and Bushes. Water Bodies include Open Water and Swamps. The entire ROIs cover a total of more than 38,000 pixels, which is more than enough to build a regression model. These ROIs will also be used in the process of accuracy assessment or model validation.

For simplicity, we can ignore the parameters α_i and β_i in the exponential equation (8). In other words, the value of these two parameters is set to 1. So the formula looks like this:

$$\rho_i' = e^{\left(\frac{\rho_i}{(\rho_i + \rho_{ca})}\right)} \quad (10)$$

For practical purposes, equation (10) is actually sufficient to transform the spectral value of the imagery transformed by (5) to be linear with respect to the original TOA reflectance. However, for accuracy purposes, of course the parameter values α_i and β_i must be estimated accurately.

Henceforth, because we disregard linear, logarithmic, and polynomial models, and we add a simplified model (10), then in the process of testing the accuracy or validating the model we will only use three models, those are (8), (9), and (10). The results of the accuracy assessment can be seen in Table II.

Visually, the results of imagery transformation using the three models in Table II do not show a significant difference in appearance. The differences will only have an effect if we do a quantitative analysis. The appearance of radiometric enhanced imageries using an exponential model without parameters can be seen in Fig. 1, Fig. 2, Fig. 3, Fig. 4, Fig. 5, and Fig. 6.

TABLE I. RADIOMETRIC ENHANCEMENT REGRESSION MODELS

Bands	Linear Eq.	Linear R^2	Exponential Eq.	Exponential R^2	Logarithmic Eq.	Logarithmic R^2	Polynomial Eq.	Polynomial R^2	Power Eq.	Power R^2
Blue	$1.7465x - 0.6813$	0.9591	$0.0002e^{14.164x}$	0.9702	$0.8052\ln(x) + 0.7486$	0.9535	$15.255x^2 - 12.386x + 2.5801$	0.9803	$18.298x^{6.5432}$	0.9685
Green	$0.7251x - 0.2109$	0.7564	$0.0068e^{6.4174x}$	0.8817	$0.209\ln(x) + 0.3186$	0.6807	$1.6435x^2 - 0.6492x + 0.0932$	0.9287	$0.7719x^{2.2665}$	0.8300
Red	$0.613x - 0.1236$	0.9227	$0.0068e^{6.4174x}$	0.9898	$0.209\ln(x) + 0.3186$	0.8368	$1.6435x^2 - 0.6492x + 0.0932$	0.9823	$0.7719x^{2.2665}$	0.9629
NIR	$0.5524x - 0.0967$	0.8248	$0.0093e^{4.7459x}$	0.9650	$0.1837\ln(x) + 0.3608$	0.6872	$0.8297x^2 - 0.2348x + 0.0319$	0.8915	$0.5084x^{1.7287}$	0.9653
SWIR 1	$0.3797x - 0.0591$	0.5770	$0.0038e^{6.5451x}$	0.9344	$0.0569\ln(x) + 0.1737$	0.3306	$1.1515x^2 - 0.4293x + 0.0329$	0.7831	$0.2843x^{1.3072}$	0.9521
SWIR 2	$0.3971x - 0.0536$	0.7081	$0.0036e^{8.1095x}$	0.8574	$0.0334\ln(x) + 0.1033$	0.2512	$1.0436x^2 - 0.2182x + 0.018$	0.9485	$0.2051x^{1.2043}$	0.9470
Average		0.7914		0.8574		0.6233		0.8856		0.9317

a. x: enhanced bands, ln: natural logarithm, e: 2.71828182845905, Eq.: equation, R^2: coefficient of correlation

TABLE II. ACCURACY ASSESSMENT

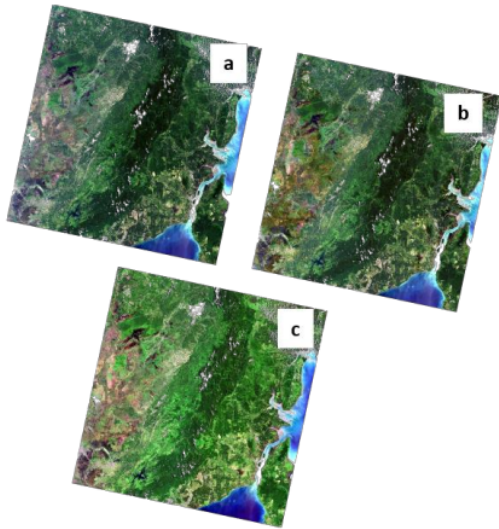| Bands	$e^{\left(\frac{\rho_i}{(\rho_i + \rho_{ca})}\right)}$ r	$e^{\left(\frac{\rho_i}{(\rho_i + \rho_{ca})}\right)}$ RMSE	$\alpha_i e^{\beta_i\left(\frac{\rho_i}{(\rho_i + \rho_{ca})}\right)}$ r	$\alpha_i e^{\beta_i\left(\frac{\rho_i}{(\rho_i + \rho_{ca})}\right)}$ RMSE	$\alpha_i \left(\frac{\rho_i}{(\rho_i + \rho_{ca})}\right)^{\beta_i}$ r	$\alpha_i \left(\frac{\rho_i}{(\rho_i + \rho_{ca})}\right)^{\beta_i}$ RMSE
Blue	0.96	1.53	0.98	0.08	0.97	0.06
Green	0.89	1.44	0.95	0.03	0.91	0.05
Red	0.97	1.3	0.99	0.02	0.98	0.02
NIR	0.93	1.72	0.95	0.04	0.94	0.04
SWIR 1	0.8	1.51	0.94	0.03	0.8	0.06
SWIR 2	0.89	1.26	0.98	0.05	0.88	0.05
Average	0.91	1.46	0.96	0.04	0.91	0.05

a. r: Pearson correlation coefficient

Fig. 1. Landsat 8 OLI imagery path/row 117/062 true color composite 4,3,2, (a) Original TOA imagery, (b) USGS TOC imagery, and (c) Radiometric enhancement imagery using exponential equation without parameter
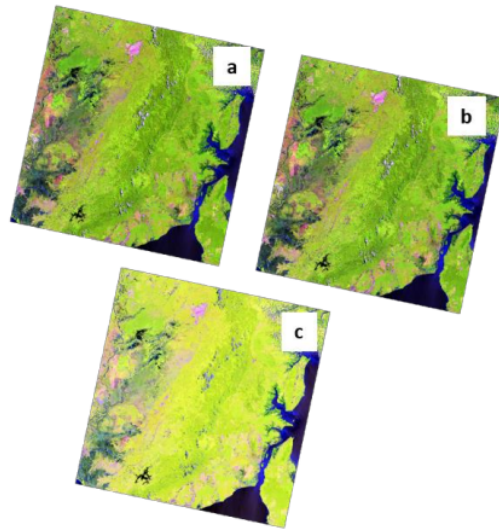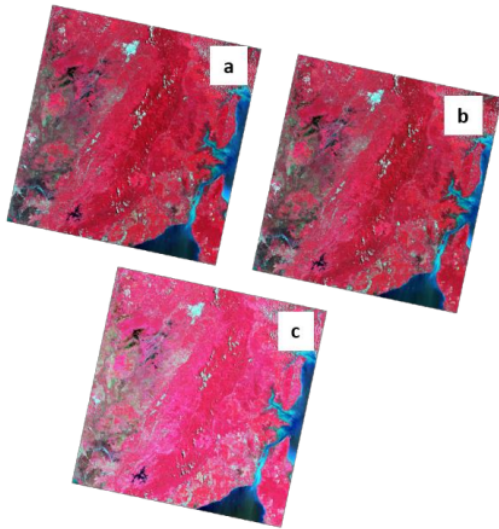

Fig. 3. Landsat 8 OLI imagery path/row 117/062 false color composite 6,5,4, (a) Original TOA imagery, (b) USGS TOC imagery, and (c) Radiometric enhancement imagery using exponential equation without parameter
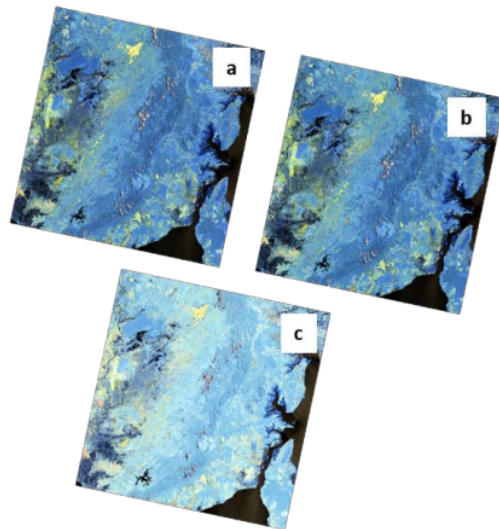

Fig. 2. Landsat 8 OLI imagery path/row 117/062 false color composite 4,3,2, (a) Original TOA imagery, (b) USGS TOC imagery, and (c) Radiometric enhancement imagery using exponential equation without parameter

Fig. 4. Landsat 8 OLI imagery path/row 117/062 false color composite 7,6,5, (a) Original TOA imagery, (b) USGS TOC imagery, and (c) Radiometric enhancement imagery using exponential equation without parameter
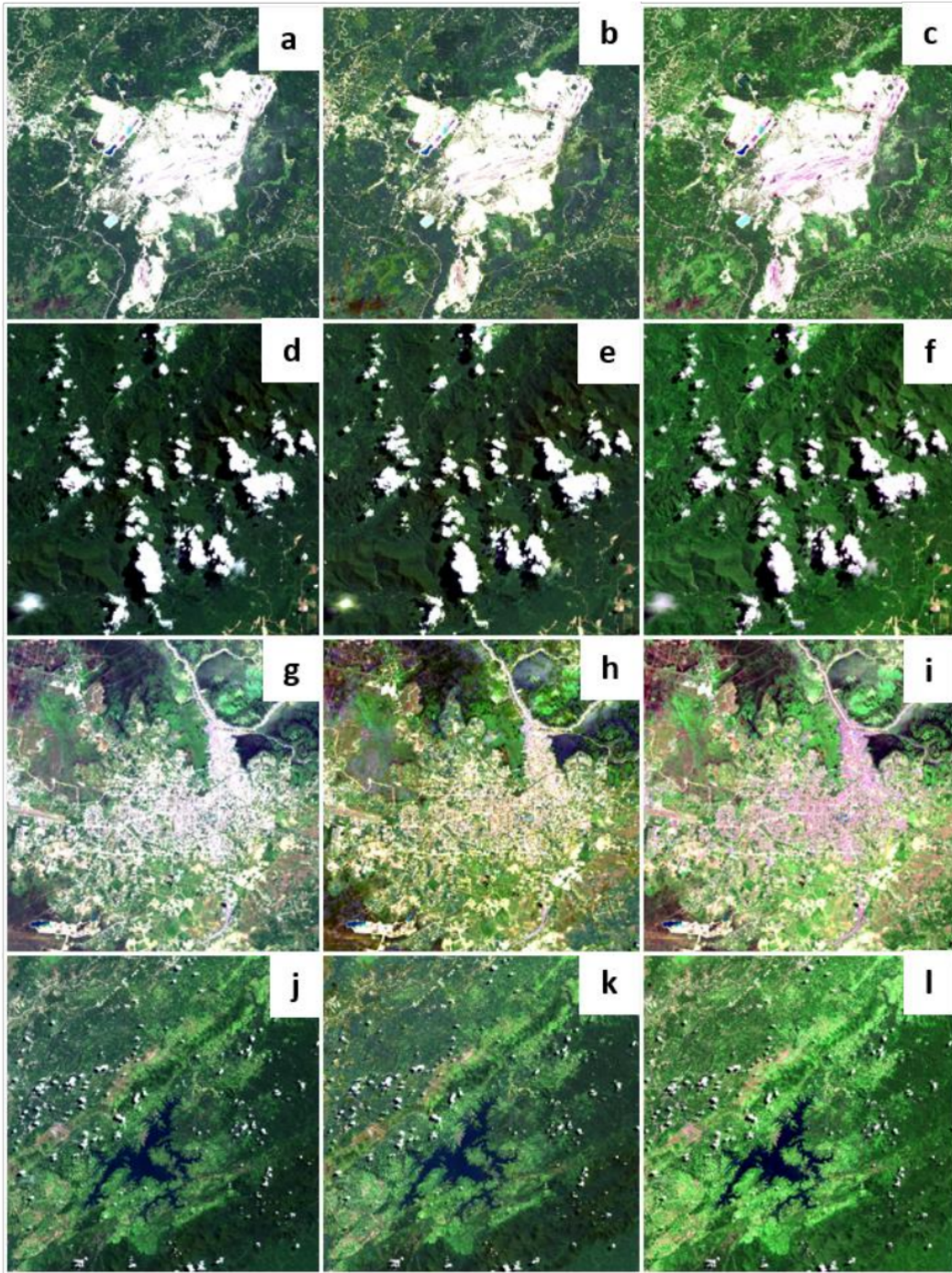
Fig. 5. Landsat 8 OLI imagery true color composite 4,3,2, (a) Bare lands in original TOA imagery, (b) Bare lands in USGS TOC imagery, (c) Bare lands in radiometric enhancement imagery using exponential equation without parameter, (d) Clouds in original TOA imagery, (e) Clouds in USGS TOC imagery, (f) Clouds in radiometric enhancement imagery using exponential equation without parameter, (g) Urban in original TOA imagery, (h) Urban in USGS TOC imagery, (i) Urban in radiometric enhancement imagery using exponential equation without parameter, (j) Water bodies and vegetation in original TOA imagery, (k) Water bodies and vegetation in USGS TOC imagery, and (l) Water bodies and vegetation in radiometric enhancement imagery using exponential equation without parameter.

Fig. 6. Urban features on Landsat 8 OLI imagery composite 4,3,2, (a) Original TOA imagery, (b) USGS TOC imagery, and (c) Radiometric enhancement imagery using exponential equation without parameter

IV. DISCUSSIONS AND CONCLUSIONS

In this research, Pearson correlation coefficient (r) was chosen as the relative accuracy assessment method to investigate the relationship between the spectral values of the enhanced bands and the bands from the USGS TOC imageries. The reason why we used the Pearson correlation coefficient to assess the accuracy of the enhanced imageries, because we assume that the spectral value of the enhanced imageries will not be exactly the same as the USGS TOC imageries. Because after all, the processing method is different. USGS TOC is processed using LaSRC.

If the Pearson correlation coefficient value is high (close to 1), it means that there is a positive linear relationship between the spectral value of the enhancement results and the USGS TOC spectral values. Furthermore, this means that the spectral value of the enhanced bands is in line with the spectral value of the USGS TOC bands.

Meanwhile, RMSE was used to compare the absolute difference between the spectral value of the enhancement results and the USGS TOC spectral values. The lower the RMSE value, the more similar the spectral value of the sharpening results is to the USGS TOC spectral values.

Based on Table II, we see that the highest accuracy is in the exponential model with parameters. This can be seen from the average value of the Pearson correlation coefficient which is the highest and the average value of the RMSE is the lowest. The high correlation in this exponential model is consistent with various research results, which test the correlation between a number of biophysical parameters with NDSI such as NDVI. Such as the Leaf Area Index (LAI) with NDVI [7][47], and Above Ground Biomass (AGB) with NDVI [45]. Therefore, basically, the correlation between the spectral value of biophysical features and NDSI such as NDVI is closer to the exponential form. Likewise with the enhancement method developed in this research.

The surprising fact is, the exponential model without parameters also gives quite accurate results, almost comparable to the power model. This is very interesting, considering that the exponential model without parameters is a very practical formula. Where no sample and parameter calculation is required in the implementation.

However, the exponential model without parameters RMSE values are quite large. This is understandable, considering the results of the transformation using the exponential model without parameters (10) will produce pixel values in the range 1 to e. To reduce the RMSE value, we can stretch the spectral value histogram into a range of 0 to 1, by using the following formula:

$$\rho_i' = \frac{e^{\left(\frac{\rho_i}{(\rho_i + \rho_{ca})}\right)} - 1}{e - 1} \quad (11)$$

Of course, stretching the spectral value histogram using (11) will reduce the practicality of the parameterless exponential model. Therefore, this technique is only intended for quantitative analysis. While for visual analysis, multispectral classification, Object-Based Image Analysis (OBIA) [42], or Geographic Object-Based Image Analysis (GEOBIA) [43], this technique is not required.

TABLE III. ACCURACY ASSESSMENT

Bands	$e^{\left(\frac{\rho_i}{(\rho_i + \rho_{ca})}\right)}$	
	r	$RMSE$
Blue	0.96	0.30
Green	0.89	0.24
Red	0.97	0.16
NIR	0.93	0.31
SWIR 1	0.8	0.26
SWIR 2	0.89	0.14
Average	0.91	0.24

Table III shows the results of the accuracy assessment of the exponential model without parameters, after the spectral values had been stretched to 0 to 1 using (11). The Pearson correlation coefficient values relatively will not change, only the RMSE values change. The RMSE values are smaller than parameterless exponential model without

stretching. But the RMSE values still not as accurate as the exponential model with parameters or power model.

Therefore, if you want to build a regression model between vegetation biomass and NDVI, for example, by using the enhanced imagery with the method developed in this research, then a more robust option is to use an exponential model with parameters or a power model. As a consequence, you have to assign a number of spectral value samples to the various spectral classes present in the imagery. These samples are needed to determine the parameters α and β in each model.

Overall, of the three models validated in Table II, the radiometric enhancement of Landsat 8 OLI imagery using the C/A band is able to provide spectral values those are close the USGS Landsat 8 OLI TOC product. This means that the method developed in this research can be used not only for visual analysis, but also for quantitative analysis. Such as the spectral value index transformation, and the like. However, for physical modeling such as using a spectral library, of course the enhancement method developed in this research is not recommended.

When observed visually on various imagery composites, the increase in visual acuity as a result of radiometric enhancement is most evident in the visible and near infrared (VNIR) bands. The increases in visual acuity referred to here are the differences in visual appearance between surface features, the more clearly visible and the easier to distinguish from one another. Such as differences in appearance between different vegetation features.

Meanwhile, on the SWIR bands, the effect is not as clear as VNIR bands. Although on the SWIR bands the surface features appear brighter overall, so that the difference in visual appearance between surface features does not change much between before and after enhancement. On the SWIR bands, the effect is quite noticeable on the cloud features. Where the clouds appear darker after radiometric enhancement, as shown in Fig. 3 and Fig. 4.

On Fig. 1, Fig 2, Fig. 3, Fig. 4, Fig. 5, and Fig. 6 visually it is clearly visible the difference in the appearance of surface features between the time before and after the enhancement. After enhancement, the surface features are more visible, even when compared to the Landsat 8 TOC. Dense vegetation, which initially looks dark on TOA and TOC, looks brighter in the enhanced imagery. So that it is visually easier to distinguish vegetation features.

While in Fig. 5, where the appearance of various thematic objects is emphasized more clearly, we can see more clearly the differences in the imageries before and after being enhanced. All imageries in Fig. 5 are true color composites of 4,3,2. Bare lands and urban, for example, can be seen more clearly the difference in color variations in the same thematic features. As we all know, this is not the case with false color composites. Whereas in the false color composite of 6,5,4 for example, all urban features will be the same color, even though the actual colors of the buildings in the field are different. Meanwhile, urban and bare lands will have the same tone/color, they differ only in texture.

Urban features are indeed the most interesting facts in this research, especially in true color composite. Where these features appear clearly increased after the enhancement process, even more clearly than USGS TOC imagery, as seen in Fig. 6. Urban features increase in sharpness while relatively maintaining the original colors of objects in the field, such as the roofs of buildings. As a result, building features are easier to distinguish from ground features visually.

In order to investigate the effect quantitatively on urban and bare land features, we can test it further using the Urban Index (UI) [26], Bare Soil Index (BI) [5], Normalized Difference Built-Up Index (NDBI) [46], Index-based Built-Up Index (IBI) [18], Normalized Difference Bareness Index. (NDBaI) [17], or Enhanced Built-Up and Bareness Index (EBBI) [4]. Especially if we want to map urban features and bare land features.

The cloud features appear slightly darker in the radiometric enhanced imagery, even in visible bands. While the haze features are quite small in size, they appear to have faded or almost disappeared. Although it needs to be tested again on imageries where the presence of haze is quite large. Of course, we can combine the enhancement method in this research with cloud correction methods from previous research, such as [8], [14], [28], or [34].

For more practical purposes later, you can even implement the method developed in this research directly on the Landsat 8 OLI Digital Number (DN). Where the pixel values of Landsat 8 OLI, which have a 16-bit radiometric resolution ranging from 0 to 65,535. This means that you don't have to first calibrate the imagery into TOA reflectance in order to use the enhancement method from this research. The results you will get will be the same as the enhancement process carried out in TOA, as in this research.

The main drawback of the method developed in this research is that we can no longer use the C/A band to be combined with other bands that have been enhanced. This is because the C/A band is used as a corrector. Therefore, if in the future you need the C/A band to be transformed with other bands, then you cannot use the enhancement method from this research. A method similar to the model developed in this research is exponential extrapolation (EXP). Where EXP is used for aerosol determination by utilizing the SWIR long wave band. The EXP method is more used for atmospheric correction of aquatic features [9][33].

Furthermore, the accuracy assessment or method validation in this research was carried out using the USGS Landsat 8 OLI TOC product, USGS Landsat 8 OLI TOC is assumed to be the spectral values of objects in the field. In other words, the closer the spectral values of the enhanced result are to the spectral values of the USGS Landsat 8 OLI TOC product, the more accurate the method will be. We recommend that further studies be carried out using samples of the spectral values of objects in the field that are measured using an image spectroradiometer.

REFERENCES

[1] A. Barnston, "Correspondence among the correlation [root mean square error] and Heidke verification measures; refinement of the Heidke score," Notes and Correspondence, Climate Analysis Center, 1992.

[2] A. Berk et al., "MODTRAN4 radiative transfer modeling for atmospheric correction," Proc. SPIE 3756, Optical Spectroscopic Techniques and Instrumentation for Atmospheric and Space Research III, (20 October 1999); https://doi.org/10.1117/12.366388

[3] A. J. Heymsfield et al., "Cirrus clouds", Meteor. Monogr., 58, 2017, pp. 2.1-2.26.

[4] A. R. As-syakur, I. W. S. Adnyana, I. W. Arthana, I. W. Nuarsa, "Enhanced Built-Up and Bareness Index (EBBI) for mapping built-up and bare land in an urban area," Remote Sensing, 4 (10), 2012, pp. 2957-2970, https://doi.org/10.3390/rs4102957.

[5] A. Rikimaru and S. Miyatake, "Development of forest canopy density mapping and monitoring model using indices of vegetation, bare soil and shadow," Proceeding of the 18th Asian Conference on Remote Sensing (ACRS) 1997, Kuala Lumpur, Malaysia, 20–25 October 1997, p. 3.

[6] B. C. Gao, "NDWI A – Normalized difference water index for remote sensing of vegetation liquid water from space," Remote Sensing of Environment, 58, 1996, pp. 257-266.

[7] B. Lee, H. Kwon, A. Miyata, S. Lindner, and J. Tenhunen, "Evaluation of a Phenology-Dependent Response Method for Estimating Leaf Area Index of Rice Across Climate Gradients," Remote Sensing, 9 (1), 2016, p. 20.

[8] C. Hu, L. Huo, Z. Zhang and P. Tang, "Multi-Temporal Landsat Data Automatic Cloud Removal Using Poisson Blending," in IEEE Access, vol. 8, pp. 46151-46161, 2020, doi: 10.1109/ACCESS.2020.2979291.

[9] D. Wang, R. Ma, K. Xue, and S. A. Loiselle, "The assessment of Landsat-8 OLI atmospheric correction algorithms for inland waters", Remote Sensing, 11 (2), 2019, p. 169.

[10] Department of the Interior United States Geological Survey (DoI USGS), "Landsat 8 (L8) data users handbook LSDS-1574 version 5.0", Department of the Interior U.S. Geological Survey, South Dakota, 2019.

[11] Department of the Interior United States Geological Survey (DoI USGS), "Landsat 8 Collection 1 (C1) land surface reflectance code (LaSRC) product guide LSDS-1368 version 3.0," Department of the Interior U.S. Geological Survey, South Dakota, 2020.

[12] D. Frantz, A. Roder, M. Stellmes, and J. Hill, "An operational radiometric landsat preprocessing framework for large-area time series applications," IEEE Trans. Geosci. Remote. Sens., 54, 2016, pp. 3928-3943.

[13] E. F. Vermote, D. Tanre, J. L. Deuze, M. Herman and J.-. Morcette, "Second Simulation of the Satellite Signal in the Solar Spectrum, 6S: an overview," in IEEE Transactions on Geoscience and Remote Sensing, vol. 35, no. 3, pp. 675-686, May 1997, doi: 10.1109/36.581987.

[14] E.H. Helmer and B. Ruefenacht, "Cloud-free satellite image mosaics with regression trees and histogram matching," Photogrammetric Engineering & Remote Sensing, Vol. 71, No. 9, September 2005, pp. 1079-1089.

[15] E. Vermote, C. Justice, M. Claverie, and B. Franch, "Preliminary analysis of the performance of the Landsat 8/OLI land surface reflectance product," Remote Sens. Environ., 185, 2016, pp. 46–56.

[16] G. M. Smith and E. J. Milton, "The use of the empirical line method to calibrate remotely sensed data to reflectance," International Journal of Remote Sensing, 1999, 20, pp. 2653-2662.

[17] H. M. Zhao and X. L. Chen, "Use of Normalized Difference Bareness Index in quickly mapping bare areas from TM/ETM+," In

[18] H. Xu, "A new index for delineating built-up land features in satellite imagery," International Journal of Remote Sensing, 29, 2008, pp. 4269-4276.

[19] H. Xu, "Modification of Normalized Difference Water Index (NDWI) to enhance open water features in remotely sensed imagery," International Journal of Remote Sensing, 27 (14), 2006, pp. 3025–3033, doi: 10.1080/01431160600589179.

[20] J. A. Richards, "Remote sensing digital imagery analysis: an introduction (fifth edition)," Springer-Verlag, Berlin, 2013.

[21] J. F. Kenney, and E. S. Keeping, "Root Mean Square," §4.15 in Mathematics of Statistics, Pt. 1, 3rd ed. Princeton, NJ: Van Nostrand, 1962, pp. 59-60.

[22] J. G. Masek et al., "A Landsat surface reflectance dataset for North America, 1990-2000," in IEEE Geoscience and Remote Sensing Letters, vol. 3, no. 1, pp. 68-72, Jan. 2006, doi: 10.1109/LGRS.2005.857030.

[23] E. J. Knight and G. Kvaran, "Landsat-8 Operational Land Imager design, characterization and performance," Remote Sensing, 6, 2014, pp. 10286-10305, doi:10.3390/rs61110286.

[24] J. W. Rouse, R. H. Haas, J. A. Schell, D. W. Deering, "Monitoring vegetation systems in the Great Plains with ERTS," Third ERTS Symposium, NASA SP-351 I, 1973, pp. 309-317.

[25] J. Wang, "Pearson correlation coefficient. In: Dubitzky W., Wolkenhauer O., Cho KH., Yokota H. (eds) Encyclopedia of Systems Biology," Springer, New York, 2013, https://doi.org/10.1007/978-1-4419-9863-7_372.

[26] M. Kawamura, S. Jayamana, and Y. Tsujiko, "Relation between social and environmental conditions in Colombo Sri Lanka and the urban index estimated by satellite remote sensing data," Int. Arch. Photogramm. Remote Sens, 31(Part B7), 1996, pp. 321-326.

[27] M. W. Matthew et al., "Status of atmospheric correction using a MODTRAN4-based algorithm. In Algorithms for Multispectral, Hyperspectral, and Ultraspectral Imagery VI," International Society for Optics and Photonics: Bellingham, WA, USA, Volume 4049, 2000, p. 199.

[28] M. Xu, X. Jia and M. Pickering, "Automatic cloud removal for Landsat 8 OLI imageries using cirrus band," 2014 IEEE Geoscience and Remote Sensing Symposium, Quebec City, QC, 2014, pp. 2511-2514, doi: 10.1109/IGARSS.2014.6946983.

[29] N. Pahlevan et al., "On-orbit radiometric characterization of OLI (Landsat-8) for applications in aquatic remote sensing," Remote Sensing of Environment, 154, 2014, pp. 272-284.

[30] P. M. Mather and M. Koch, "Computer processing of remotely-sensed Images: An Introduction, 4th Edition," John Wiley & Sons Ltd, Chichester, 2011.

[31] P. S. Chavez, "An improved dark-object subtraction technique for atmospheric scattering correction of multispectral data," Remote Sensing of Environment, 24, 1988, pp. 459-479.

[32] P. S. Chavez, "Image-based atmospheric corrections-revisited and improved," Photogrammetric Engineering and Remote Sensing, 62, 1996, pp. 1025-1036.

[33] Q. Vanhellemont and K. Ruddick, "Advantages of high quality SWIR bands for ocean colour processing: Examples from Landsat-8," Remote Sens. Environ., 2015, 161, pp. 89-106.

[34] R. Cao, Y. Chen, J. Chen, X. Zhu, and M. Shen, "Thick cloud removal in Landsat images based on autoregression of Landsat time-series data," Remote Sensing of Environment, Volume 249, November 2020, 112001, https://doi.org/10.1016/j.rse.2020.112001.

[35] R. Richter, "A spatially adaptive fast atmospheric correction algorithm," International Journal of Remote Sensing, 1996, 17, pp. 1201-1214.

[36] R. T. Wilson, "Py6S: A Python interface to the 6S radiative transfer model," Comput. Geosci., 2013, 51, p. 166.

[37] S. K. McFeeters, "The use of the Normalized Difference Water Index (NDWI) in the delineation of open water features", International Journal of Remote Sensing, 17 (7), 1996, pp. 1425-1432.

[38] S. Saunier and A. Northrop, "Landsat 8, Level 1 Product Performance Cyclic Report – July 2016," LS08 Quality Report, IDEAS+, Telespazio VEGA, Issue July 2016, 1 September 2016.

[39] S. Sterckx et al., "OPERA: An atmospheric correction for land and water," In Proceedings of the Sentinel-3 for Science Workshop, Venice, Italy, 2–5 June 2015.

[40] S. Y. Kotchenova and E. F. Vermote, "Validation of a vector version of the 6S radiative transfer code for atmospheric correction of satellite data. Part II. Homogeneous Lambertian and anisotropic surfaces," Applied Optics, Vol. 46, No. 20, 10 July 2007, pp. 4455-4464.

[41] S. Y. Kotchenova, E. F. Vermote, R. Matarrese, and F. J. Klemm Jr., "Validation of a vector version of the 6S radiative transfer code for atmospheric correction of satellite data. Part I: Path radiance," Applied Optics, Vol. 45, No. 26, 10 September 2006, pp. 6762-6774.

[42] T. Blaschke, "Object based image analysis for remote sensing," ISPRS Journal of Photogrammetry and Remote Sensing, 65, 2010, pp. 2-16.

[43] T. Blaschke et al., "Geographic Object-Based Image Analysis – Towards a new paradigm," ISPRS Journal of Photogrammetry and Remote Sensing, 87, 2014, pp. 180-191.

[44] T. Lillesand, R. W. Kiefer, and J. Chipman, "Remote sensing and imagery interpretation, 7th edition", John Wiley & Sons, Inc., Hoboken, NJ, 2015.

[45] X. Zhang et al., "An evaluation model for aboveground biomass based on hyperspectral data from field and TM8 in Khorchin grassland, China," PLoS ONE, 15 (2), 2020, p. e0223934.

[46] Y. Zha, J. Gao, and S. Ni, "Use of normalized difference built-up index in automatically mapping urban areas from TM imagery," International Journal of Remote Sensing, 24, 2003, pp. 583-594.

[47] Y. Zhang et al., "An integrated algorithm for estimating regional latent heat flux and daily evapotranspiration," International Journal of Remote Sensing, 27 (1-2), 2006, pp. 129-152.

[48] Z. Zhang, G. He, and X. Wang, "A practical DOS model-based atmospheric correction algorithm," International Journal of Remote Sensing, 31 (11), 2010, pp. 2837-2852.

Radiometric Enhancement of Landsat 8 OLI Imagery Using Coastal/Aerosol Band

8 acp.copernicus.org
Internet Source
<1%

9 www.researchgate.net
Internet Source
<1%

10 www.science.gov
Internet Source
<1%

11 Nima Pahlevan, Zhongping Lee, Jianwei Wei, Crystal B. Schaaf, John R. Schott, Alexander Berk. "On-orbit radiometric characterization of OLI (Landsat-8) for applications in aquatic remote sensing", Remote Sensing of Environment, 2014
Publication
<1%

12 I Sumantri, A Sulaiman, N Gulo, P Wahyuni. "Effects of curcumin supplementation in aflatoxin B1-contaminated diet on the performance and egg quality of laying duck", IOP Conference Series: Earth and Environmental Science, 2019
Publication
<1%

13 arxiv.org
Internet Source
<1%

14 core.ac.uk
Internet Source
<1%

15 umr144.curie.fr
Internet Source
<1%

16   Concha, Javier A., and John R. Schott. "Retrieval of color producing agents in Case 2 waters using Landsat 8", Remote Sensing of Environment, 2016.
Publication   <1%

17   J.M. Ramírez-Cuesta, R.G. Allen, P.J. Zarco-Tejada, A. Kilic, C. Santos, I.J. Lorite. "Impact of the spatial resolution on the energy balance components on an open-canopy olive orchard", International Journal of Applied Earth Observation and Geoinformation, 2019
Publication   <1%

18   dspace.unitus.it
Internet Source   <1%

19   www.spiedigitallibrary.org
Internet Source   <1%

20   Ahmed AKAKBA, Belkacem Lahmar. "The applications of geomatics to predicate forest fire based on earlier pre-fire conditions. A case study: Belezma national park -Algeria", Research Square Platform LLC, 2022
Publication   <1%

21   Handbook of Satellite Applications, 2013.
Publication   <1%

22   Johannes Rosentreter, Ron Hagensieker, Björn Waske. "Towards large-scale mapping of local climate zones using multitemporal Sentinel 2

data and convolutional neural networks",
Remote Sensing of Environment, 2020
Publication

23   Nima Pahlevan, Sudipta Sarkar, Sadashiva   <1 %
      Devadiga, Robert E. Wolfe, Miguel Roman, Eric
      Vermote, Guoqing Lin, Xiaoxiong Xiong.
      "Impact of Spatial Sampling on Continuity of
      MODIS–VIIRS Land Surface Reflectance
      Products: A Simulation Approach", IEEE
      Transactions on Geoscience and Remote
      Sensing, 2017
      Publication

24   Yingjie Li, Jing Chen, Qingmiao Ma, Hankui K.   <1 %
      Zhang, Jane Liu. "Evaluation of Sentinel-2A
      Surface Reflectance Derived Using Sen2Cor in
      North America", IEEE Journal of Selected
      Topics in Applied Earth Observations and
      Remote Sensing, 2018
      Publication

25   journals.plos.org   <1 %
      Internet Source

26   mdpi.com   <1 %
      Internet Source

27   tsukuba.repo.nii.ac.jp   <1 %
      Internet Source

28   Ronald C. Estoque, Yuji Murayama.   <1 %
      "Classification and change detection of built-

up lands from Landsat-7 ETM+ and Landsat-8 OLI/TIRS imageries: A comparative assessment of various spectral indices", Ecological Indicators, 2015
Publication

29	Syamani D. Ali, Ichsan Ridwan, Meldia Septiana, Abdi Fithria et al. "GeoAI for Disaster Mitigation: Fire Severity Prediction Models using Sentinel-2 and ANN Regression", 2022 IEEE International Conference on Aerospace Electronics and Remote Sensing Technology (ICARES), 2022 Publication	<1 %
30	Yang, Aixia, Bo Zhong, Wenbo Lv, Shanlong Wu, and Qinhuo Liu. "Cross-Calibration of GF-1/WFV over a Desert Site Using Landsat-8/OLI Imagery and ZY-3/TLC Data", Remote Sensing, 2015. Publication	<1 %
31	jorlrodriguezg.github.io Internet Source	<1 %
32	josh.yosh.org Internet Source	<1 %
33	law.resource.org Internet Source	<1 %
34	rc.library.uta.edu Internet Source	<1 %

35 technicalgeography.org
Internet Source
<1 %

36 www.itc.nl
Internet Source
<1 %

37 www.tandfonline.com
Internet Source
<1 %

38 Pietro Ceccato, Nadine Gobron, Stéphane Flasse, Bernard Pinty, Stefano Tarantola. "Designing a spectral index to estimate vegetation water content from remote sensing data: Part 1", Remote Sensing of Environment, 2002
Publication
<1 %

39 Wang, Yingjie, Liangyun Liu, Yong Hu, Donghui Li, and Zhengqiang Li. "Development and validation of the Landsat-8 surface reflectance products using a MODIS-based per-pixel atmospheric correction method", International Journal of Remote Sensing, 2016.
Publication
<1 %

40 S. E. El-Hendawy, W. M. Hassan, Y. Refay, U. Schmidhalter. "On the use of spectral reflectance indices to assess agro-morphological traits of wheat plants grown under simulated saline field conditions", Journal of Agronomy and Crop Science, 2017
<1 %

Publication

Exclude quotes	On	Exclude matches	Off
Exclude bibliography	On		